low-field MR extrapolated to $H = 0$, MR* shows roughly a factor of 3 enhancement observed for all temperatures (Fig. 4). This enhancement appears to correlate with the larger effective intergrain barrier formed by the annealing process discussed earlier. This suggests that the description of transport at the grain boundaries evolves from a field-dependent scattering process to tunneling with increasing ρ and MR.

Our study of polycrystalline films provides a new candidate for high-MR media. In recent years, there has been much interest in magnetoresistive oxides and artificial structures derived from them. Although very important for achieving and understanding new physical properties, examples requiring epitaxial multilayer growth are unlikely to be directly transferred to applications because of the high cost of preparation. By comparison, polycrystalline films of CrO_2 readily grow on a wide range of substrates, and annealing steps can greatly improve the intergrain properties by using surface-decomposed Cr_2O_3 as a tunnel barrier. Thus, the materials aspects of polycrystalline films of CrO_2 appear to be quite attractive for possible applications. The predominant issue to be resolved is the origin of the rapid decrease in MR* with increasing temperature, which is quite similar to that observed in polycrystalline perovskite manganites and thin-film trilayer tunnel junctions of perovskite manganites (*3*, *5*). Is this temperature dependence intrinsic, or can it be raised to higher temperatures by improving the materials interface properties (controlling impurity states, for example), in analogy to the successful development of magnetic metallic multilayers as useful room-temperature devices after the initial discovery of giant MR at low temperatures (*15*)? Our results demonstrate the promise of a nanocomposite materials engineering approach for designing useful MR properties, and perhaps for addressing this important question.

Fig. 4. The magnetoresistance (MR) of the two polycrystalline films (film I, solid lines; film II, dashed lines). (**Inset**) The field-dependent ρ at 5 K normalized to the maximum value. The main panel displays the temperature dependence of the magnitude of the low-field MR extrapolated to $H = 0$, MR*.

REFERENCES AND NOTES

1. R. A. de Groot, F. M. Mueller, P. G. van Engen, K. H. J. Buschow, *Phys. Rev. Lett.* **50**, 2024 (1983).
2. M. K. Gubkin, T. M. Perekalina, A. V. Bykov, V. A. Chubarenko, *Phys. Solid State* **35**, 728 (1993).
3. H. Y. Hwang, S.-W. Cheong, N. P. Ong, B. Batlogg, *Phys. Rev. Lett.* **77**, 2041 (1996).
4. T. Kimura *et al*., *Science* **274**, 1698 (1996).
5. J. Z. Sun *et al*., *Appl. Phys. Lett.* **69**, 3266 (1996).
6. H. Y. Hwang and S.-W. Cheong, unpublished results.
7. V. A. Vas'ko *et al.*, *Phys. Rev. Lett.* **78**, 1134 (1997).
8. K. Schwarz, *J. Phys. F* **16**, L211 (1986).
9. K. P. Kämper, W. Schmitt, G. Güntherodt, R. J. Gambino, R. Ruf, *Phys. Rev. Lett.* **59**, 2788 (1987).
10. R. Wiesendanger, H.-J. Güntherodt, G. Güntherodt, R. J. Gambino, R. Ruf, *ibid.* **65**, 247 (1990).
11. B. L. Chamberland, *CRC Crit. Rev. Solid State Mat. Sci.* **7**, 1 (1977).
12. B. Kubota and E. Hirota, *J. Phys. Soc. Jpn.* **16**, 345 (1960).
13. D. S. Chapin, J. A. Kafalas, J. M. Honig, *J. Phys. Chem.* **69**, 1402 (1965).
14. D. S. Rodbell, J. M. Lommel, R. C. DeVries, *J. Phys. Soc. Jpn.* **21**, 2430 (1966).
15. See, for example, P. M. Levy, *Science* **256**, 972 (1992).

16. We thank B. Barber for assistance with the SEM studies, and B. Batlogg and Y. Suzuki for helpful discussions.

2 August 1997; accepted 22 October 1997

Imaging of Intermittency in Ripple-Wave Turbulence

William B. Wright, R. Budakian, D. J. Pine,* S. J. Putterman†

The dynamics of a fluid surface filled with high-amplitude ripples were studied with a technique (diffusing light photography) that resolves the height at all locations instantaneously. Even when nonlinearities are strong enough to generate a (Kolmogorov) cascade from long wavelength (where energy is input) to shorter wavelength, the resulting turbulent state contains large coherent spatial structures. The appearance of these structures in a thermal equilibrium state (with the same average energy) would be highly improbable.

An attempt to distill into one question the issue that has intrigued scientists about the turbulent motion of fluids is, How does fully developed turbulence differ from thermal noise with the same energy? (*1*). To address this issue, we used diffusing light images of a strongly rippled surface to quantify the competition between structure formation and randomization of energy in far-off equilibrium fluid motion that must be contained in a unified theory of turbulence.

Thermal equilibrium differs from turbulence in that thermal equilibrium is global whereas the spectrum of turbulence has end points. Turbulence is driven by an external source of energy that enters at long wavelengths and then, through nonlinear interactions, cascades through an inertial region of shorter wavelengths until the energy reaches a wavelength that is so small that viscosity dominates the motion (*2*–*4*).

In the steady state, the spectrum of energy in thermal equilibrium and in the inertial range of turbulence are both power laws in the wavenumber k. For example, the equilibrium distribution of thermal energy for capillary waves per unit area of surface per range of wavenumber is

$$u(k) \approx (k_B T)k \qquad (1)$$

which expresses the equipartition of energy (k_B is Boltzmann's constant and T is temperature). In comparison the steady-state wave turbulent distribution of ripple energy driven by a source of power per unit area q is

$$u(k) \approx q^{1/2}(\rho\sigma)^{1/4}k^{-7/4} \qquad (2)$$

where ρ is the fluid density and σ is the surface tension (*5*–*7*). [For vortex turbulence as analyzed by Kolmogorov, $u(k) \sim \rho^{1/3}q^{2/3}k^{-5/3}$ where q is now the power input per unit of volume by the tides into the stirring of the seas (*3*, *4*, *8*, *9*).]

The challenges posed by turbulence are much deeper than the need to explain the different values for the exponent of k in the equilibrium (Eq. 1) and far-from-equilibrium (Eq. 2) steady states. The distinct physical aspects of turbulence are to be found in the fluctuations around the steady state. Because motion is characterized by phase as well as amplitude, the spectra (Eqs. 1 and 2) do not uniquely determine the state of fluid motion to

Physics Department, University of California, Los Angeles, CA 90095, USA.

*Present address: Department of Chemical Engineering, University of California, Santa Barbara, CA 93106, USA.
†To whom correspondence should be addressed.

which they apply. In thermal equilibrium the phases randomize so precisely that fluctuations are exponentially suppressed. The probability that a measurement of energy at wavenumber k finds a power different from the average (Eq. 1) is proportional to the exponent of the difference and so follows a Gaussian distribution (in amplitude), with the result that large fluctuations are highly improbable. In turbulence, large fluctuations are not exponentially suppressed (*4*, *10*, *11*), and the broad-band power spectrum (Eq. 2) masks the spontaneous, intermittent appearance of large, coherent structures.

Diffusing light photography (DLP) provides a means to image the spatial structure of intermittency in ripple-wave turbulence. Such a structure is displayed in Fig. 1, which is a plot of the local rate of dissipation of mechanical energy into heat within the turbulent range of motion for capillary waves. In the turbulent regime, the fluid motion is concentrated into areas of high amplitude that substantially exceed the root-mean-square (rms) value. Furthermore, these regions of high dissipation are organized into large structures.

In DLP, the instantaneous height $\zeta(x, y)$ of a fluid surface with large variations in height and curvature can be measured (*7*). The fluid is illuminated from below with a 10-μs flash of light that diffuses through the water as a result of multiple scattering from a suspension of 1-μm polystyrene spheres whose concentration (0.04%) is large enough to render the water milky but small enough not to affect the viscosity. The light intensity that exits the upper surface depends on the local depth: Less light penetrates deeper surfaces. Application of the calibration curve in Fig. 2A (inset), pixel by pixel, to a charge-coupled device (CCD) camera photo of the upper surface (Fig. 3A) leads to a rendering of the surface height (Fig. 3B).

Key to the usefulness of this technique is the elimination of ray crossings that occur when light is refracted by a surface of varying slope. For example, a light front that approaches a peak in the fluid-air interface from below will be refracted toward that peak and cross other rays just above the interface. These caustics prevent the use of shadowgraphs (*12*) for measuring $\zeta(x, y)$ accurately. Faraday (*13*) was the first to notice that the addition of milk to water eliminated caustics and rendered a smoothly varying pattern of transmitted light. Figure 4 shows a cross section of an image of a sine wave mold made from a solution of water, polyballs, and gelatin. The circles represent the reconstructed surface obtained with DLP. For this surface, rays from a horizontal light front (shadowgraph) would cross 2 mm above the maxima. The diffusing-light rendition is faithful even though the slopes vary from +1 to −1. For surface waves, the slope is the Mach number, which in our experiments reached maximum values comparable to those that characterize this mold.

Also shown in Fig. 4 is the three-quarter width of a laser beam as a function of distance traveled in the polyball suspension. The laser is depicted here as incident from above. The light will propagate a transport mean free path, l^*, before diffusion causes the beam to spread. A higher concentration of scatterers leads to a smaller l^*. The diffusing light technique works when l^* is comparable to or greater than ζ but less than the overall depth, L, of the fluid ($L > l^* > \zeta$; for surfaces with a large radius of curvature the technique can work even when $l^* < \zeta$). In our experiments, the container of fluid is illu-

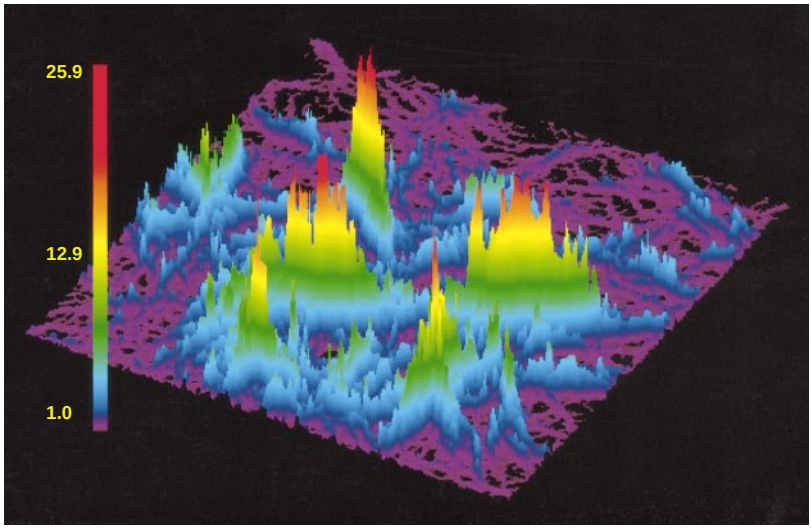

Fig. 1. Experimental data for the rate of dissipation of turbulent ripple motion into heat as a function of location on the surface. Energy is injected into capillary wave motion at 25 Hz (k = 6.4 cm^{-1}, λ = 0.98 cm) through parametric excitation. The motion obeys the applicable Kolmogorov power spectrum in the wavenumber range 15 cm^{-1} < k < 60 cm^{-1}. From the instantaneously measured surface height, the contribution to the local rate of dissipation in a subrange Δk (here 42.4 cm^{-1} < k < 46.5 cm^{-1} so λ ≈ 1.4 mm) is obtained by digital filtering and then plotted in dimensionless form. The displayed region is 7.56 cm by 7.56 cm. Blue regions correspond to the rms value of dissipation and red regions correspond to over 20 times this value. Large, organized structures are readily apparent. In general, adjoining subranges of k, from the same image, have different structures.

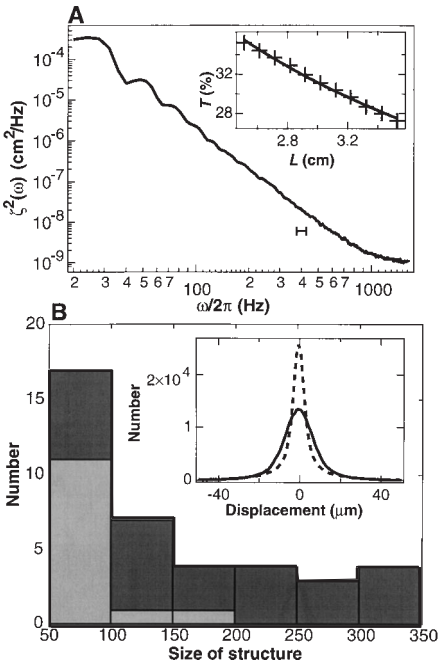

Fig. 2. (**A**) The frequency spectrum of ripple turbulence. The region in which the data were filtered to obtain the graph (B) is indicated. (A, inset) A typical calibration curve for transmission, T, of light through water with a suspension of neutrally buoyant polystyrene spheres (index of refraction of 1.6, concentration 0.04%). The depths, L, span the experimental range. For this concentration, a light ray travels about 0.5 mm before Mie scattering from a polyball. Because the scattering angle is small (about 20° on average), the ray must undergo more than 10 scattering events in order to be turned through a large angle. Transmission through the "milky" water is approximately given by $T = \frac{5}{3}l^*/(L + \frac{4}{3}l^*)$ (*22*). (**B**) The distribution of structures in turbulence. The number of pixels with a common side required to cover those regions where the dissipation exceeds 5 rms for 10 photos of turbulence. The light-shaded histogram denotes randomized phases. The dark-shaded histogram denotes actual data. (Inset) The distribution of heights for a real (dashed line) and phase-randomized photo. The randomized data, but not the physical state, fit well to a Gaussian distribution.

minated uniformly from below and a camera is focused onto the surface to record the transmitted light. The light reaching an individual pixel on the CCD comes from inside the cone (Fig. 4). If l^* is too small, the beam spreads so rapidly that light collected from one point is affected by the overall surface shape and the method fails to yield a useful image.

The power spectrum $[u(k)]$ of the turbulent state, obtained from the spatial Fourier transform of ζ (Fig. 3A), is found to be isotropic and broad band in the range $15\ \text{cm}^{-1} < k < 60\ \text{cm}^{-1}$. The exponent (-2.2 ± 0.1) is close to that given in Eq. 2 (*7*, *14*). Use of the ripple dispersion law, $\omega^2 = (\sigma/\rho)k^3$, implies that the range of frequencies, $\omega/2\pi$, for which this motion is turbulent is $76\ \text{Hz} < f < 630\ \text{Hz}$, as we find from the temporal Fourier transform of $\zeta(t)$ of the motion in a 200-μm region of the surface (Fig. 2A).

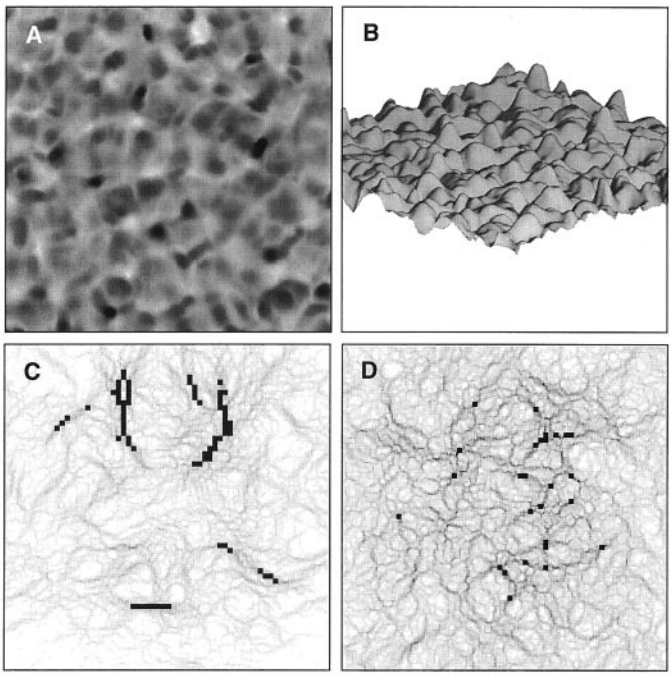

Fig. 3. Diffusing light photography and analysis of turbulent capillary waves. (**A**) Display of an actual photo obtained with a Princeton Instruments CCD with 65,000 gray scales and 1024 by 1024 pixels binned into 512 by 512 super-pixels. The displayed area (7.56 cm by 7.56 cm) spans 256 by 256 super-pixels. (**B**) Rendering of the surface height as a function of location, $\zeta(x, y)$, on the plane of the undisturbed surface. The rms amplitude of motion is 1.5 mm. (**C**) The dissipation function (Eq. 3) of (A) filtered to retain only those components in the subrange Δk (the data have also been median filtered). Those squares of 16 super-pixels that exceed 80 rms are blackened to exhibit structure in turbulence. The width of these structures is approximately the wavelength spanned by the subrange Δk. This is a different image from that used for Fig. 1. (**D**) Comparison with (C) where, in addition to filtering, the phases of the various Fourier components have been randomized. Although the power spectrum is completely unaffected, the area of structures as well as the regions of low amplitude are greatly diminished.

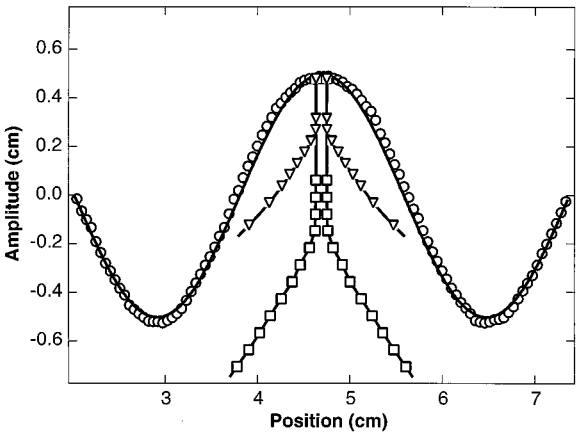

Fig. 4. Experimental criteria for DLP. Our measurement of l^* is overlaid on a calibrated image of a sinusoidal mold. Shown is the width of a He-Ne laser beam (633 nm) propagating into the liquid (squares denote a 0.04% solution and triangles denote a 0.12% solution). The indicated beam width contains 75% of the light. For the 0.04% solution, the beam propagates ballistically for a distance equal to the transport mean free path ($l^* \approx 0.75$ cm) before spreading. For a 0.04% solution, light propagates into the bulk of the medium without interacting with other surface locations. In this instance the calibration curve in Fig. 2 can be used to obtain an accurate rendering of the mold from a photo of the transmitted light. For a 0.12% solution the beam probes nearby points on the surface, and so when its calibration curve is applied to a cross section of the mold, the rendered height is wrong at the peaks (but not the troughs) by 25%. For a 0.3% polyball suspension, the peaks are overestimated by a factor of 2.

To elucidate structure in the turbulent state, images such as that in Fig. 3A are digitally filtered in a fixed range of wavenumbers (in this instance, $42.4\ \text{cm}^{-1} < k < 46.5\ \text{cm}^{-1}$) that lie entirely within the region of broad-band motion (the corresponding frequency range 373 to 429 Hz is indicated in Fig. 2A). Then, the local rate of dissipation, $\dot{E}$, of wave energy into heat by molecular viscosity is plotted in dimensionless form (Fig. 1) as

$$\dot{E}\lambda_0^2/\sigma\nu \approx (\lambda_0\nabla^2\zeta)^2 \qquad (3)$$

where ν is the kinematic viscosity and λ_0 is the wavelength at which energy is injected.

Quantifying structure within turbulence requires algorithms sensitive to the local response. Such algorithms are more akin to the JET Cluster routines (*15*) of high-energy experimental physics than various global correlation functions. In this vein, we measure the size of intermittent structures by first blackening those units of 16 pixels where the average dissipation exceeds the rms value by a factor of 5 (Fig. 3C). This is compared to a computer-simulated noise image where the spectrum has been preserved but the phases have been randomized (Fig. 3D). These data show that turbulent motion within a narrow range of wavelengths is characterized by large fluctuations (*16*). This is demonstrated by the presence of organized high-amplitude structures as well as large regions where the motion is remarkably quiescent. The spectrum of the Kolmogorov cascade (which is a global correlation) expresses a remarkable balance of these disparate motions.

Figure 2B (inset) shows the distribution of amplitudes of the two images, from which we derive the local dissipation (Fig. 3, C and D). Although their standard deviation (rms power) is the same, lack of random phasing in the physically realized broad-band turbulent state accounts for its non-Gaussian form and also for the broad distribution of localized structures (Fig. 2B). There exists no theory for this key characteristic of turbulent motion (*17*).

Our observation of intermittency stands in contrast with the conclusions based on computer simulations (*18*) that ripple turbulence is well described by a deterministic Boltzmann type of kinetic equation. We propose that the shortage of modes that can be dealt with in a computer calculation accounts for the differing conclusions. The parameter of merit for the extent to which a system displays turbulence (*7*) is the ratio of the rate $1/\tau$ of nonlinear interactions to the spacing between the lowest lying modes ω_G. For computer calculations with 256 by 256 modes this ratio is about 1, whereas for the

15 cm by 15 cm resonator used in our experiments, the ratio is about 10,000 (*19*). It has been emphasized that as τ decreases (so that the system becomes more turbulent), the effects of intermittency should become more pronounced (*20, 21*). It is unclear whether the nature of the observed structures will change at higher levels of energy throughput or as viscous interactions with the boundaries are modified. An improved system for the study of ripple turbulence is the surface of a levitated sphere of fluid. In this instance, waves scatter only from each other and not a boundary.

REFERENCES AND NOTES

1. W. Heisenberg, *Proc. R. Soc. London Ser. A* **195**, 402 (1948).
2. L. F. Richardson, *Weather Prediction by Numerical Process* (Cambridge Univ. Press, Cambridge, 1922); *Proc. R. Soc. London Ser. A* **110**, 709 (1926).
3. A. N. Kolmogorov, *Dokl. Akad. Nauk. SSSR* **30**, 301 (1941); A. M. Oboukhov; *ibid.* **32**, 19 (1941).
4. L. D. Landau and E. M. Lifshitz, *Fluid Mechanics* (Pergamon, New York, 1955).
5. V. E. Zakharov, V. S. L'vov, G. Falkovich, in *Kolmogorov Spectra of Turbulence* (Springer Berlin, 1992), pp. 33–230.
6. R. Z. Sagdeev, *Rev. Mod. Phys.* **51**, 1 (1979).
7. W. B. Wright, R. Budakian, S. J. Putterman, *Phys. Rev. Lett.* **76**, 4528 (1996); W. B. Wright, thesis, University of California, Los Angeles (1996).
8. H. L. Grant, R. W. Stewart, A. Moilliet, *J. Fluid Mech.* **12**, 241 (1961).
9. U. Frisch and S. Orszag, *Phys. Today* (January 1990), p. 24.
10. A. M. Oboukhov, *J. Fluid Mech.* **13**, 77 (1962).
11. A. N. Kolmogorov, *ibid*., p. 82.
12. B. Christianson, P. Alstrom, M. Levinsen, *Phys. Rev. Lett.* **68**, 2157 (1992); B. J. Gluckman, P. Marq, J. Bridges, J. P. Gollub, *ibid.* **71**, 2034 (1993).
13. M. Faraday, *Trans. R. Soc*. (1831), p. 299.
14. DLP allows us to independently measure the frequency and wavenumber spectra without invoking strong assumptions such as the Taylor hypothesis [S. G. Saddoughi and S. V. Veeravalli, *J. Fluid Mech.* **268**, 333 (1994).].
15. M. H. Seymour, *Z. Phys.* **C62**, 127 (1994); S. Catani, *Phys. Lett.* **B269**, 432 (1991); W. Bartel *et al*., *Z. Phys.* **C33**, 23 (1986); G. Arnison *et al*., *Phys. Lett.* **B123**, 115 (1983); C. Albajar *et al*., *Nucl. Phys.* **B309**, 405 (1988).
16. C. Foias, O. P. Manley, R. Temam, *Phys. Fluids* **A3**, 898 (1991).
17. R. H. Kraichnan, *Bull. Am. Phys. Soc.* **42**, 53 (1997).
18. A. N. Pushkarev and V. E. Zakharov, *Phys. Rev. Lett.* **76**, 3320 (1996).
19. Even for such a low density of modes, these simulations (*18*) were able to generate the Kolmogorov spectrum.
20. R. H. Kraichnan, in *Turbulence and Stochastic Processes*, J. C. R. Hunt, O. M. Phillips, D. Williams, Eds. (Royal Society, London, 1991); *Phys. Fluids* **10**, 2080 (1967).
21. The issue being addressed here is intermittency in fully developed turbulence, not intermittency in the transition to turbulence [D. J. Tritton, in *Physical Fluid Dynamics* (Van Nostrand Reinhold, New York, 1977), pp. 13–16].
22. P. D. Kaplan, M. H. Kao, A. G. Yodh, D. J. Pine, *Appl. Opt.* **32**, 3828 (1993). The effect of surface slope on the transmission coefficient for diffusing light has been calculated by M. U. Vera and D. J. Durian [*Phys. Rev.* **E53**, 3215 (1996)] and D. J. Durian [*ibid.* **E50**, 857 (1994)].

23. We acknowledge valuable discussions with D. Durian, P. H. Roberts, B. I. Halperin, S. Garrett, R. Keolian, and the Lund high-energy physics group. This research is supported by the U.S. Department of Energy (Division of Engineering and Geophysics) and by NASA (Microgravity Research).

8 August 1997; accepted 17 October 1997

IRAK (Pelle) Family Member IRAK-2 and MyD88 as Proximal Mediators of IL-1 Signaling

Marta Muzio,* Jian Ni, Ping Feng, Vishva M. Dixit†

The interleukin-1 receptor (IL-1R) signaling pathway leads to nuclear factor kappa B (NF-κB) activation in mammals and is similar to the Toll pathway in *Drosophila*: the IL-1R–associated kinase (IRAK) is homologous to Pelle. Two additional proximal mediators were identified that are required for IL-1R–induced NF-κB activation: IRAK-2, a Pelle family member, and MyD88, a death domain–containing adapter molecule. Both associate with the IL-1R signaling complex. Dominant negative forms of either attenuate IL-1R–mediated NF-κB activation. Therefore, IRAK-2 and MyD88 may provide additional therapeutic targets for inhibiting IL-1–induced inflammation.

After binding to IL-1, the IL-1R type I (IL-1RI) associates with the IL-1R accessory protein (IL-1RAcP) and initiates a signaling cascade that results in the activation of NF-κB (*1*–*6*). Substantial similarity exists between the IL-1R signaling pathway in mammals and the Toll signaling pathway in *Drosophila*. Toll shares sequence homology with the cytoplasmic domain of the IL-1RAcP and induces Dorsal activation (a homolog of NF-κB) via the adapter protein Tube and the protein kinase Pelle (*7*–*10*). The recently identified IRAK (IL-1R–associated kinase) is homologous to Pelle (*11*). However, in mammalian cells, additional complexity is thought to exist, because of the observation that multiple protein kinase activities coprecipitate with the IL-1RI (*12, 13*). Furthermore, given that in *Drosophila* the adapter protein Tube interacts with and regulates Pelle's activity, it is likely that analogous adapter or regulatory molecules might participate in IL-1 signaling.

In order to identify putative additional protein kinases associating with the IL-1R signaling complex, expressed sequence tag databases were searched for sequences homologous to IRAK (*14, 15*). A novel partial human cDNA was identified that showed significant homology, by Clustall alignment analysis, to both IRAK and Pelle. Screening of a human umbilical vein endothelial cell cDNA library resulted in the isolation of a full-length cDNA clone; analysis of the nucleotide sequence revealed an open reading frame encoding a 590–amino acid protein with a calculated size of 65 kD (Fig. 1A). Given its sequence and functional similarity to IRAK, the molecule was designated IRAK-2. Northern (RNA) blot analysis revealed a single IRAK-2 transcript expressed in a variety of tissues whose size (about 4 kb) was consistent with that of the cDNA (Fig. 1B).

Ectopic expression of IRAK-2 induced NF-κB activation as determined by the relative luciferase activity of an NF-κB–responsive construct. Truncated versions encoding amino acids 1 to 96 [IRAK-2(1-96)] and amino acid 97 to the COOH-terminal end [IRAK-2(97-590)] failed to induce any luciferase activity, which suggests that the integrity of the molecule was essential for its function (Fig. 2A). Deletional analysis has previously shown that an NH_2-terminal truncated version of Pelle analogous to IRAK-2(97-590) is also inactive, which leads to the suggestion that Pelle's recruitment to the plasma membrane through its NH_2-terminal domain is necessary for its subsequent function (*7*). Thus, we tested whether IRAK-2(1-96) or IRAK-2(97-590) could act as dominant negative inhibitors of IL-1R–induced NF-κB activity. Coexpression of IL-1RI and IL-1RAcP (here called IL-1Rs for clarity) strongly induced NF-κB activity. Surprisingly, both IRAK-2(1-96) and IRAK-2(97-590) inhibited IL-1Rs–induced NF-κB activity. A dominant negative mutant version of the downstream kinase NIK that is implicated in IL-1R–

M. Muzio and V. M. Dixit, University of Michigan Medical School, Department of Pathology, Ann Arbor, MI 48109, USA.
J. Ni and P. Feng, Human Genome Sciences, Rockville, MD 20850–9998, USA.

*Present address: Mario Negri Institute, Milano, Italy.
†To whom correspondence should be addressed. Present address: Genentech, South San Francisco, CA 94080, USA. E-mail: dixit@gene.com